

Numerical Simulation of Low-Density Shock-Wave Interactions

Christopher E. Glass
Langley Research Center, Hampton, Virginia

The NASA STI Program Office ... in Profile

Since its founding, NASA has been dedicated to the advancement of aeronautics and space science. The NASA Scientific and Technical Information (STI) Program Office plays a key part in helping NASA maintain this important role.

The NASA STI Program Office is operated by Langley Research Center, the lead center for NASA's scientific and technical information. The NASA STI Program Office provides access to the NASA STI Database, the largest collection of aeronautical and space science STI in the world. The Program Office is also NASA's institutional mechanism for disseminating the results of its research and development activities. These results are published by NASA in the NASA STI Report Series, which includes the following report types:

- **TECHNICAL PUBLICATION.** Reports of completed research or a major significant phase of research that present the results of NASA programs and include extensive data or theoretical analysis. Includes compilations of significant scientific and technical data and information deemed to be of continuing reference value. NASA counterpart and peer-reviewed formal professional papers, but having less stringent limitations on manuscript length and extent of graphic presentations.
- **TECHNICAL MEMORANDUM.** Scientific and technical findings that are preliminary or of specialized interest, e.g., quick release reports, working papers, and bibliographies that contain minimal annotation. Does not contain extensive analysis.
- **CONTRACTOR REPORT.** Scientific and technical findings by NASA-sponsored contractors and grantees.

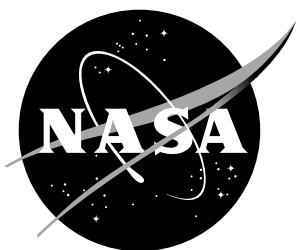
- **CONFERENCE PUBLICATION.** Collected papers from scientific and technical conferences, symposia, seminars, or other meetings sponsored or co-sponsored by NASA.
- **SPECIAL PUBLICATION.** Scientific, technical, or historical information from NASA programs, projects, and missions, often concerned with subjects having substantial public interest.
- **TECHNICAL TRANSLATION.** English-language translations of foreign scientific and technical material pertinent to NASA's mission.

Specialized services that complement the STI Program Office's diverse offerings include creating custom thesauri, building customized databases, organizing and publishing research results... even providing videos.

For more information about the NASA STI Program Office, see the following:

- Access the NASA STI Program Home Page at ***<http://www.sti.nasa.gov>***
- E-mail your question via the Internet to help@sti.nasa.gov
- Fax your question to the NASA STI Help Desk at (301) 621-0134
- Phone the NASA STI Help Desk at (301) 621-0390
- Write to:
NASA STI Help Desk
NASA Center for Aerospace Information
7121 Standard Drive
Hanover, MD 21076-1320

NASA/TM-1999-209358



Numerical Simulation of Low-Density Shock-Wave Interactions

Christopher E. Glass
Langley Research Center, Hampton, Virginia

National Aeronautics and
Space Administration

Langley Research Center
Hampton, Virginia 23681-2199

July 1999

Available from:

NASA Center for AeroSpace Information (CASI)
7121 Standard Drive
Hanover, MD 21076-1320
(301) 621-0390

National Technical Information Service (NTIS)
5285 Port Royal Road
Springfield, VA 22161-2171
(703) 605-6000

1 Introduction

An important issue for the design and development of aerospace vehicles is the effect of various types of flow phenomena on aerodynamic performance and aeroheating characteristics. Of particular concern are shock-wave interactions, which can cause significant local increase in surface pressure and heating, especially from Types III and IV interference patterns (See Edney [3]). To quantify the effects, experiments and computational studies have been performed at continuum flow conditions (e.g., Holden et al. [4]); however, relatively few results have been presented for the low density, rarefied–transitional flow environment (See Carlson and Wilmoth [2] and Pot et al. [6]).

The experimental conditions of low-density, Mach 10 shock-wave interaction tests (Pot et al. [6]), performed at the ONERA R5Ch hypersonic wind tunnel, provide a baseline condition for the present computational study of various shock-wave interactions. In the experiment, a wedge at a 20° angle-of-attack produced a planar incident shock wave, which interacted with the bow shock of a 0.008m radius instrumented cylinder aligned with its axis parallel with the plane of the incident shock. The experiment produced various shock-wave interference patterns, depending on the relative position of the incident and bow shock waves. A schematic diagram of the experimental test configuration is shown in Fig. 1.

The purpose of this paper is to explore several topics. Primarily, is Computational Fluid Dynamics (CFD) adequate to predict shock-wave interactions for a low-density, transitional–rarefied free-stream condition? In particular, can the Type IV interference pattern and its surface interaction be predicted with confidence? Also, at continuum conditions, some experiments of the Type IV interference pattern have shown it to be unsteady (Holden et al. [4]). In the present study, time-accurate CFD is employed to examine flow steadiness at the low-density condition.

The paper is organized as follows: First, a general discussion of the various types of shock-wave interference patterns is presented. Emphasis is placed on the Type III, Type IV, and Type V patterns because they cause the greatest augmentation of pressure and heating on a blunt leading edge subjected to shock-wave interaction. Second, the numerical technique used to predict the shock-wave interference patterns and cylinder surface properties is dis-

cussed. Third, an analysis of the numerical results are presented and some comparisons are made with the experimental results for the Type IV shock-wave interference. Fourth, the maximum pressure and heating as a function of incident shock position is presented to map the surface effects from the low-density shock-wave interactions. Finally, a discussion of a time-accurate solution for the Type IV interference is presented.

2 Shock-Wave Interference

Edney [3] categorized six shock-wave interference patterns and the type of surface interaction caused by each pattern that occur when a weak oblique shock wave intersects a bow shock at various locations about its periphery. Features of the flow field reveal the physical mechanisms that cause these interference patterns. Although each interference pattern is discussed in detail by Edney [3], a brief description of the inviscid features of the Type III, Type IV, and Type V patterns is given subsequently in this section (see Fig. 2) because these three interference patterns have higher surface pressure and heating associated with them than the others; hence, the physical mechanism, which affects the surface, is important to quantify.

The shock-wave interference pattern is determined by the location where the incident and bow shock waves intersect, the strength of the incident shock, and the angle on the blunt leading-edge surface with respect to the impinging shear layer (See Edney [3].).

2.1 Type III interference pattern

The Type III interference is caused by the intersection of shocks of opposite families when a weak incident shock intersects a bow shock inside the subsonic region near the sonic point. This occurs in the lower subsonic region for the Type III interference pattern as shown in Fig. 3. The left running incident shock wave turns the free-stream flow upward to region 3 and intersects the bow shock wave. Behind the intersection point, the flow in regions 2 and 4 are at the same pressure and are turned at the same flow angle. The flow is subsonic in region 2 and supersonic in region 4, and these two regions are separated by a shear layer, which attaches to the wall boundary layer causing a shear-layer–boundary-layer interaction. The interaction maximum heating

depends on the impingement angle, θ_5 , between the shear layer and the wall, the pressure rise of the weak shock between regions 4 and 5, and whether the attaching shear layer is laminar or turbulent.

2.2 Type IV interference pattern

The Type IV interference pattern is caused by the intersection of either shocks of opposite families or shocks of the same family. The intersection point of the incident shock and bow shock can be above or below the normal-shock portion of the bow shock as shown schematically in Fig. 2. However, both result in a Type IV interference pattern, which is shown in Fig. 4.

Referring to Fig. 3, when the wall turning angle is greater than the maximum turning angle for region 4 to produce supersonic flow in region 5, the Type III interference transitions to Type IV. The transition occurs as the incident shock intersects closer to the normal-shock portion of the bow shock. The onset of the Type IV interference becomes apparent with the formation of a well-defined supersonic jet embedded within the subsonic regions between the bow shock wave and the surface. The supersonic jet is separated by shear layers from the subsonic flow in regions 2 and 5, as shown in Fig. 4, and impinges on the blunt leading edge.

The flow process up to region 4 is identical to the Type III interference. However, for the Type IV interference, supersonic flow in region 4 is turned through a weak left-running wave to region 6. Flow in region 6 matches flow direction and pressure with the subsonic flow in region 5. Supersonic flow from region 6 to region 7 is expanded through a Prandtl-Meyer expansion fan to match the pressure in region 2. Supersonic flow is recompressed from region 7 to region 8 through a series of left running waves to match again the pressure in region 5. Weak compression of the flow in the jet and then strong compression through the jet bow shock results in high localized pressure and heating at the wall stagnation point.

2.3 Type V interference pattern

The Type V interference pattern occurs when the incident shock wave intersects the bow shock just above the upper sonic point for the orientation shown in Fig. 5. Both shock waves are of the same family. A supersonic jet is present for the Type V interference; however, the jet is much thinner than

the Type IV supersonic jet. The Type V jet turns away from the surface, dissipates, and does not impinge on the surface.

The flow that affects the surface is initially compressed to region 2 through the weak, left-running incident shock wave. Then, flow in region 2 is compressed to region 3 by flow deflection to match the leading-edge wall turning angle. The flow in region 3 is supersonic. A requirement of the flow in regions 4 and 5 is that the pressure and flow turning angles must match at the shear layer, which separates them. Therefore, region 3 flow is compressed to region 5 through a right-running wave to match the pressure and flow direction in region 4. Note that the flow in region 4 is subsonic. The right-running shock wave that impinged on the wall boundary layer results in the shock-wave-boundary-layer interaction at the wall, which causes increased pressure and heat transfer.

3 Numerical technique

Flow conditions of a low-density shock-wave interaction study (Pot et al. [6]), performed in the ONERA R5Ch hypersonic wind tunnel at Mach 10 in air, are used as an inflow boundary condition for the present numerical study. The free-stream flow conditions are $T_\infty = 52.5\text{K}$ and $p_\infty = 5.9\text{ Pa}$ resulting in a length Reynolds number, $Re_L = 167,000/\text{m}$ and a Knudsen number, $Kn_D = 0.01$ based on the 0.016m cylinder diameter.

To approximate the inflow boundary condition for the computational domain, oblique shock relations were applied to air modeled as a perfect gas flow over a sharp leading edge 20° wedge resulting in the flow properties downstream of the wedge shock. The inflow boundary of the computational domain was then described by the properties of the free stream and post-wedge shock, with the discontinuity at the oblique shock wave location. To change the interaction type, the flow property discontinuity was translated about the outer computational boundary, which is equivalent to varying the dimension y_{IS} shown in Fig. 1. The wall temperature was assumed constant at 300K and the outflow boundary condition was interpolated from the interior cells.

For the laminar computations, the Reynolds-averaged Navier-Stokes equations are applied to flow conditions, which match the experiment, with the *GASP* CFD code (See AeroSoft [1].), a commercially available flow solver.

Air was modeled as a perfect gas. The full geometry of the experimental test apparatus (wedge and cylinder) was not modeled numerically – the computational domain contained the flow field about the forward portion of the cylinder, which captured the shock-wave interference region. To fully capture the various interference patterns, a 361 x 181 node grid extended normally from the surface nine body radii above and below the cylinder and seven body radii forward of the cylinder. Circumferential grid spacing for the 360 cells at the wall boundary is one-half degree, and radial spacing from the wall outward varied geometrically from about 0.01mm to about 1mm at the outer inflow boundary. A Type IV interference calculation on a 361 x 361 grid produced the same result as on the 361 x 181 node grid; therefore, 180 cells normally distributed from the surface was deemed adequate for the present calculations.

Employing the computational domain described above, time-accurate solutions of the Reynolds-averaged Navier-Stokes equations were obtained with third-order Roe flux splitting normal and van Leer flux splitting lateral to the cylinder surface. The solution was advanced in time using Jacobi time integration until the solution L_2 norm was reduced to a constant value with mesh sequencing. Typically, the L_2 norm was reduced about 9 orders of magnitude before a solution was considered converged.

4 Results and Discussion

Shock-wave interaction solutions of different interference patterns were obtained for the grid described in Section 3 by changing the value of y_{IS} from 0.5mm to 12.5mm. In this section, selected results from those solutions are presented. The interference flow field of the Type III, Type IV, and Type V patterns are shown first. Next, surface pressure and heating resulting from the three patterns are presented and discussed. Then, the extent of the Type IV interference as a function of y_{IS} for the present flow conditions is examined. Finally, flow steadiness of the Type IV interference is explored.

4.1 Interference patterns

Computed flow-field solutions are presented as density gradient contours. The density gradient contours, which show the structure of a shock-wave

interference pattern, are compared with the patterns given by Edney [3] to help characterize the interference type.

Shown in Fig. 6 is the density gradient of the flow field for $y_{IS} = 3.2\text{mm}$. The shock-wave structure shown in the figure is that of the Type III interference pattern. As discussed in Section 2.1, the Type III results when a weak incident shock intersects a bow shock and causes the shear layer, which separates the subsonic region behind the bow shock from the supersonic flow processed through the incident shock, to attach to the surface of the blunt leading edge. The density gradient explicitly shows the shear layer attachment.

As the value of y_{IS} is varied to 9.9mm , the Type III transitions to a Type IV interference as shown in Fig. 7. The density gradient shows distinctly the supersonic jet of the Type IV interference. Note that the density gradient of the flow field shows that for this condition, the supersonic jet is terminated at region 7 (See Fig. 4.). In addition, the terminal shock of the supersonic jet is shown in Fig. 7. Adjacent to the jet terminal shock on the blunt leading edge is the location of the highest surface pressure and heating. The bow shock standoff for the undisturbed cylinder was in good agreement with the DSMC result of Moss et al. [5]; however, the shock standoff for the Type IV interference is about twice the DSMC value (Moss et al. [5]) (DSMC shock standoff matches experimental results of Pot et al. [6].).

By further increasing the incident shock location to $y_{IS} = 11.6\text{mm}$, the interference pattern is changed to Type V as shown in Fig. 8. The supersonic jet for this case is swept above the blunt leading edge surface and dissipates. Heating and pressure increase is caused by shock-wave–boundary-layer interaction at the surface as discussed previously.

4.2 Effect of interference on surface properties

Circumferential surface pressure and heating distributions from the computations at three different incident shock wave positions about the outer computational boundary are shown in Fig. 9(a) and (b), respectively. Pressure and heating rate given in the figure are normalized by calculated cylinder stagnation line values for undisturbed flow based on the free stream conditions where $p_o = 760\text{ Pa}$ and $q_o = 59.2\text{ kW/m}^2$, which are within 0.1% and 2.6%, respectively, of \mathcal{GASP} undisturbed flow values. The $\theta = 0^\circ$ position

indicated on the figure refers to stagnation line with the positive direction above and negative below the cylinder stagnation line (Also, see Fig. 1.). The interactions that are shown on the figure are labeled as Types III, IV, and V, based on the calculated flow field features shown previously and the surface profile distributions as compared with those published earlier, e.g., see Edney [3] and Holden et al. [4].

Because the present numerical results did not include the incident shock-wave generator in the calculation, the location of the incident shock wave with respect to the cylinder for the comparison with the experimental results for the Type IV interference was chosen based on aligning the numerical and experimental pressure distributions. Shown in Fig. 9(a) is the comparison between the numerical and experimental pressure distributions for the Type IV interference. The CFD computation predicts a higher maximum pressure than the experiment. Moss et al. [5] also predict pressure higher than the experiment; however, their calculated pressure is 32% lower than the CFD. Also, the pressure domain of the CFD about the peak is broader than the DSMC. The greater shock standoff distance of the CFD supports a wider supersonic jet, which affects a larger region on the cylinder.

Shown in Fig. 9(b) are the numerical heating rate predictions for the Type III, IV, and V interference and the experimental results of Pot et al. [6] for the Type IV. The comparison of the Type IV heating results shows that for the experiment, inadequate gauge spacing prevents both the maximum heating value and heat transfer gradients to be measured adequately. Maximum heating presented by Moss et al. [5] for this interaction is 15% higher than the CFD.

For the purpose of comparison, maximum heating from the CFD in Fig. 9(b) is presented with a correlation given by Holden et al. [4] in Fig. 10 where maximum normalized heating (heating enhancement factor) is given as a function of the rarefaction parameter, $M_\infty/Re_p^{1/2}$. The present computational result (given by the solid circle) fits well with the data of Holden et al. [4] (given by the open squares); i.e., the maximum Type IV interference heating from CFD agrees with the correlation.

The maximum pressure, normalized by the stagnation line pressure, and the location of the maximum pressure on the cylinder as a function of the dimension y_{IS} (see Fig. 1) is shown in Fig. 11. For the results given in the figure, y_{IS} varies from 0.5mm to 12.5mm to show the maximum pressure for 24

numerical simulations. Inspection of the flow field and surface distributions showed that the Type IV interference exists for $3.9\text{mm} \leq y_{\text{IS}} \leq 11.7\text{mm}$, and for $y_{\text{IS}} > 11.7\text{mm}$, the transition to Type V interference is abrupt with a sharp pressure decrease.

4.3 Time-accurate shock-wave interference

The temporal behavior of the Type IV shock-wave interference for the low-density ONERA R5Ch hypersonic wind tunnel condition is presented and discussed in this section. The initial condition of the time-accurate solution was a bow shock about the cylinder, which was produced by numerically integrating the free-stream flow condition to steady-state convergence. To begin the time-accurate solution, an incident shock wave was introduced as an inflow boundary condition of the computational domain. A constant time step of 1×10^{-8} sec was applied to integrate the solution. Normalized maximum pressure and its location are presented as a function of time in Fig. 12. For zero time, p_{max}/p_o equals 1 and θ at $p_{\text{max}} = 0^\circ$. As time advances, note that it takes $0.3 \mu\text{sec}$ for the incident shock-wave interaction to affect the surface pressure. Between $0.5 \mu\text{sec}$ and $5 \mu\text{sec}$, the pressure remains relatively constant and the location of the peak pressure changes from -19° to 3.5° . Next, between $5 \mu\text{sec}$ and $7.5 \mu\text{sec}$, the Type IV interference pattern settles to near its steady value. From $7.5 \mu\text{sec}$ to $10 \mu\text{sec}$ the interference oscillates until for $t > 10 \mu\text{sec}$, $p_{\text{max}}/p_o = 14.1$ and θ (at p_{max}) $\approx -23^\circ$. The figure shows that the low-density interacting flow solution becomes steady for $t > 10 \mu\text{sec}$. The numerical procedure was continued for a total of $15 \mu\text{sec}$ to assure a steady-state condition was obtained. Moreover, Fig. 12 shows that the startup process for the Type IV occurs quickly for this case in $10 \mu\text{sec}$.

5 Conclusions

Results of present CFD calculations of low-density shock-wave interactions are presented as flow-field density gradients and surface pressure and heating distributions. Flow-field density gradients show complex shock interactions of the Type III, IV, and V interference patterns that match those given by Edney [3]. Although the undisturbed bow shock standoff compared well, for the Type IV interference, the CFD bow shock standoff distance is about

twice that of the DSMC given by Moss et al. [5]. The surface pressure and heating resulting from these interacting flows are also presented; and, for the Type IV interference pattern, a comparison with experimental data is shown. The maximum surface pressure from the CFD is greater by a factor of two than the experiment and greater than the DSMC prediction of Moss et al. [5]. Comparison of maximum heating shows the CFD result is less than that from DSMC. Further study is needed to resolve discrepancies between the two results for the Type IV interference.

The maximum pressure and location of the maximum pressure are shown as a function of incident shock-wave location with respect to the cylinder. The Type IV interference pattern is present over the range of incident shock positions, i.e., $3.9\text{mm} \leq y_{IS} \leq 11.7\text{mm}$. A time-accurate solution of the Type IV interference revealed that the flow is steady after an initial transient to establish the shock interaction, which occurred within $10\mu\text{sec}$.

References

- [1] AeroSoft, Inc. (1996) *GASP* Version 3, The General Aerodynamic Simulation Program User Manual. AeroSoft, Inc., Blacksburg, Virginia.
- [2] Carlson AB, Wilmoth RG (1992) Shock interference prediction using direct simulation Monte Carlo. *Journal of Spacecraft and Rockets* 29-6: 780–785.
- [3] Edney B (1968) Anomalous heat transfer and pressure distributions on blunt bodies at hypersonic speeds in the presence of an impinging shock. FFA Report 115, Stockholm, Sweden.
- [4] Holden M, Sweet S, Kolly J, Smolinski G (1998) A review of the aerothermal characteristics of laminar, transitional and turbulent shock/shock interaction regions in hypersonic flows. AIAA 98-0899.
- [5] Moss JN, Pot T, Chananetz B, Lefebvre M (1999) DSMC simulation of shock/shock interactions: emphasis on type IV interactions. 22nd International Symposium on Shock Waves.
- [6] Pot T, Chananetz B, Lefebvre M, Bouchardy P (1998) Fundamental study of shock/shock interference in low density flow: flowfield mea-

surements by DLCARS. 21st International Symposium on Rarefied Gas Dynamics.

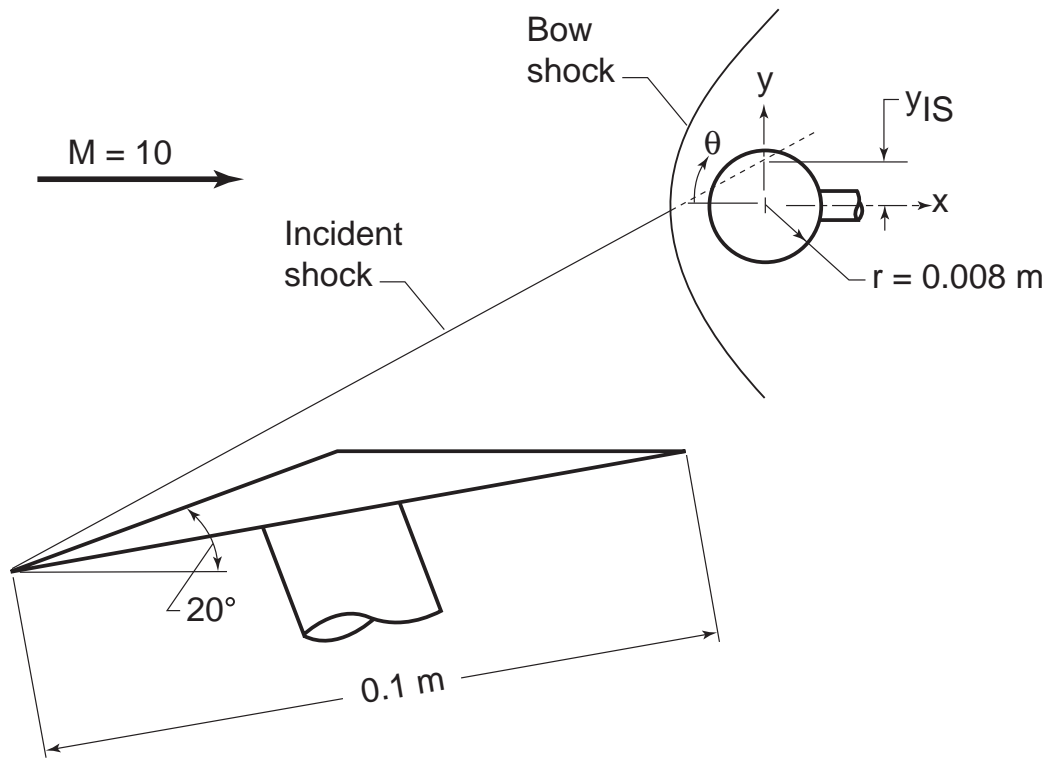


Figure 1: Schematic diagram of ONERA shock-wave interaction test configuration.

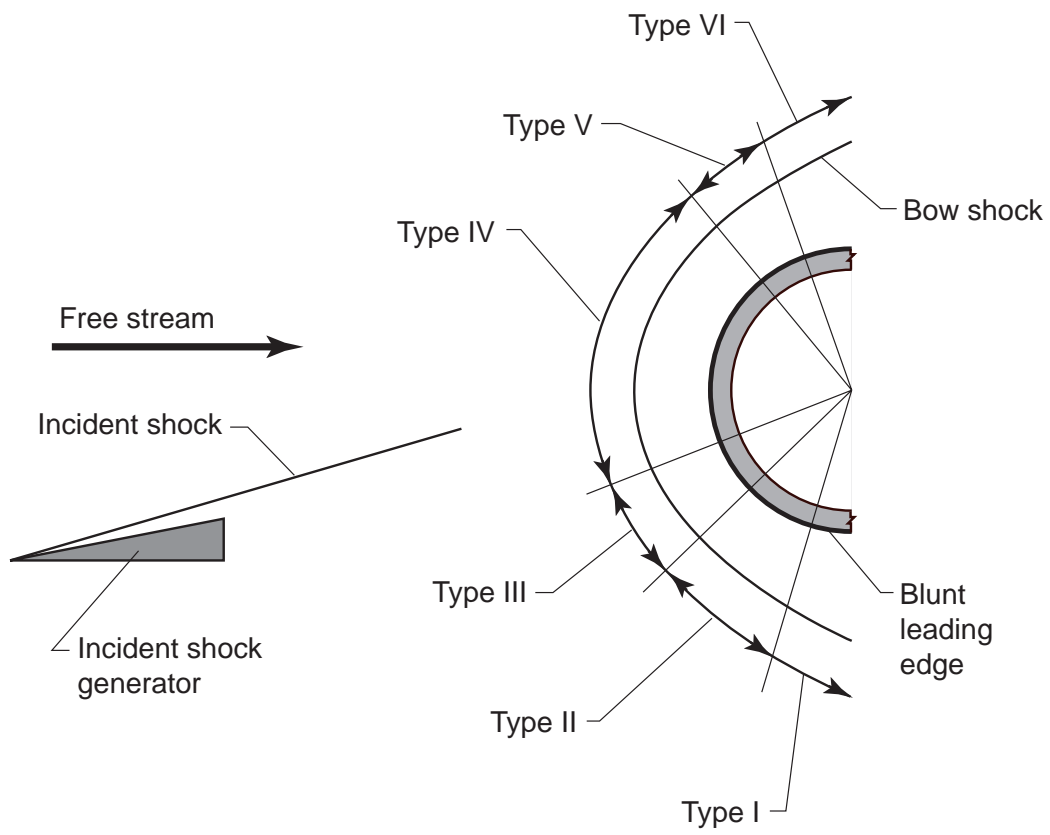


Figure 2: Location of six shock-wave interference patterns on blunt leading edge.

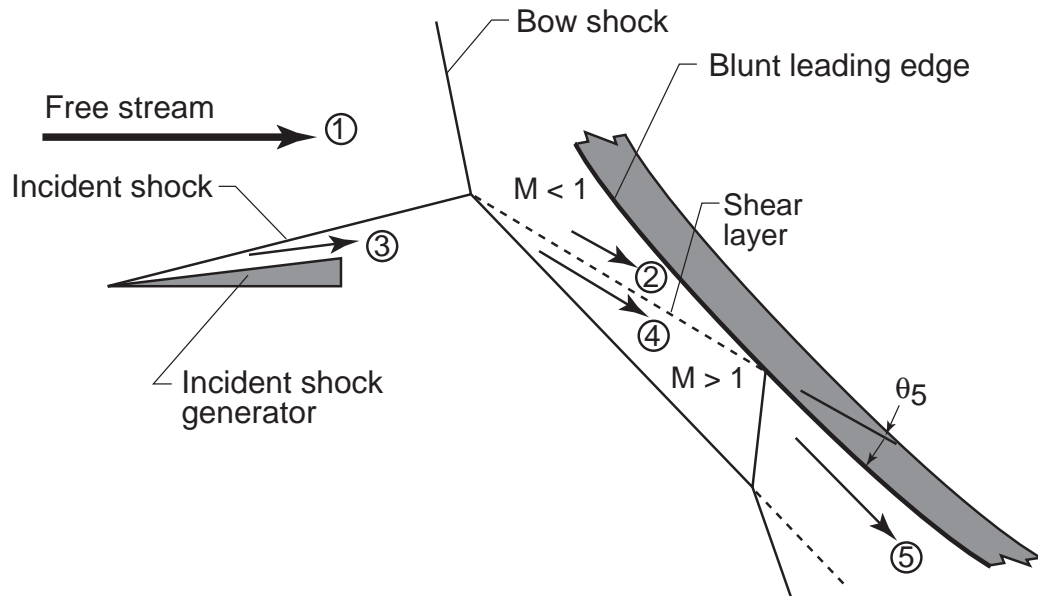


Figure 3: Type III interference pattern.

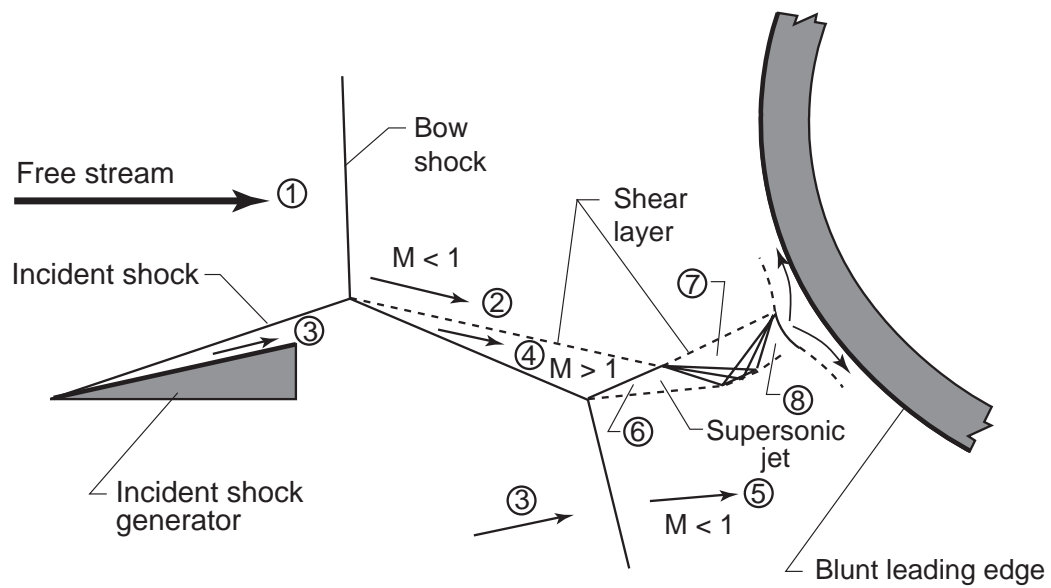


Figure 4: Type IV interference pattern.

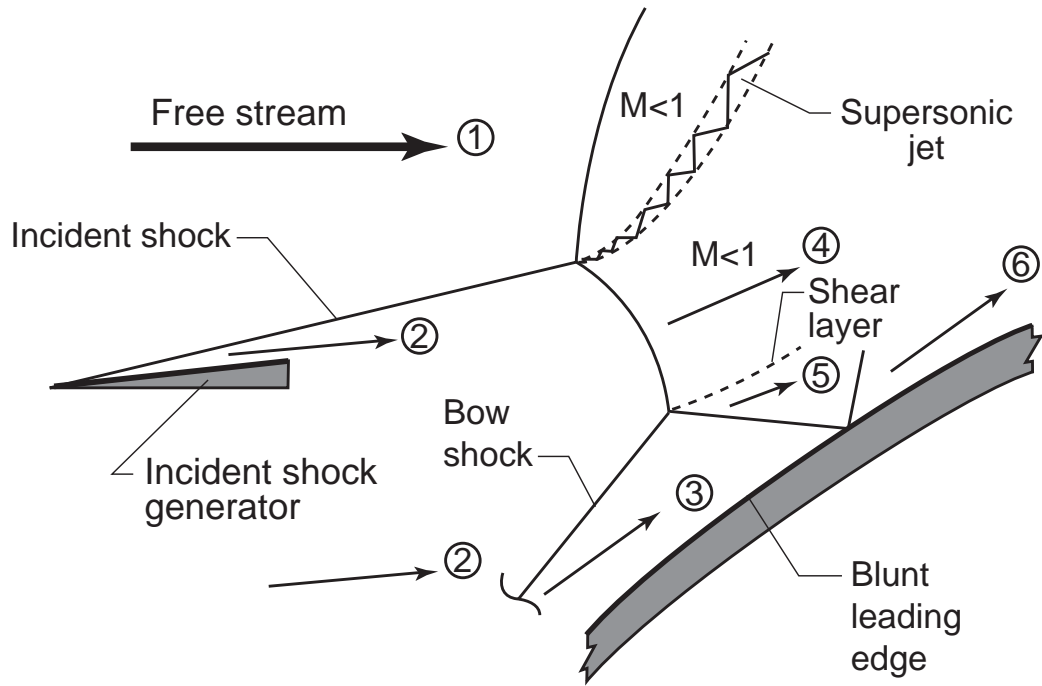


Figure 5: Type V interference pattern.

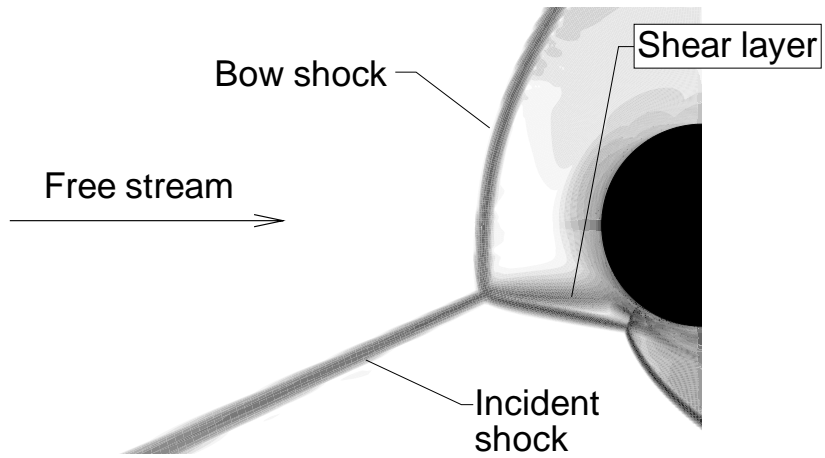


Figure 6: Flow field density gradient of Type III interference ($y_{IS} = 3.2\text{mm}$).

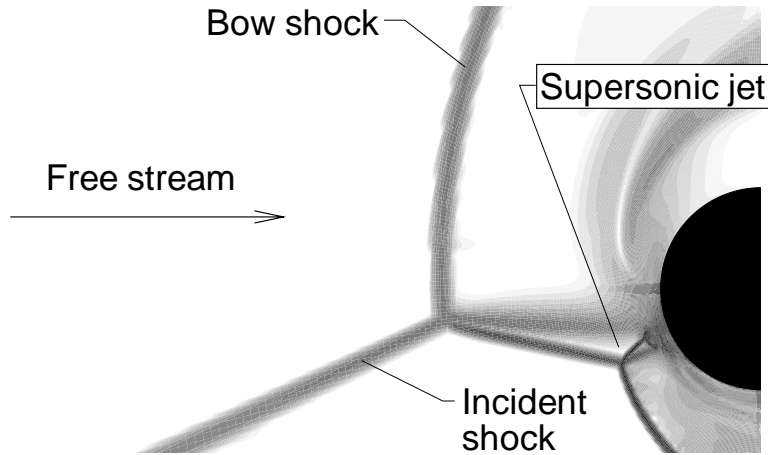


Figure 7: Flow field density gradient of Type IV interference ($y_{IS} = 9.9\text{mm}$).

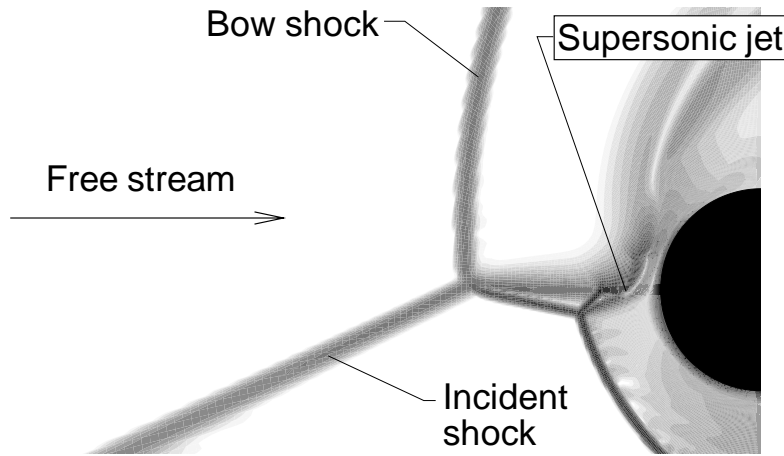


Figure 8: Flow field density gradient of Type V interference ($y_{IS} = 11.6\text{mm}$).

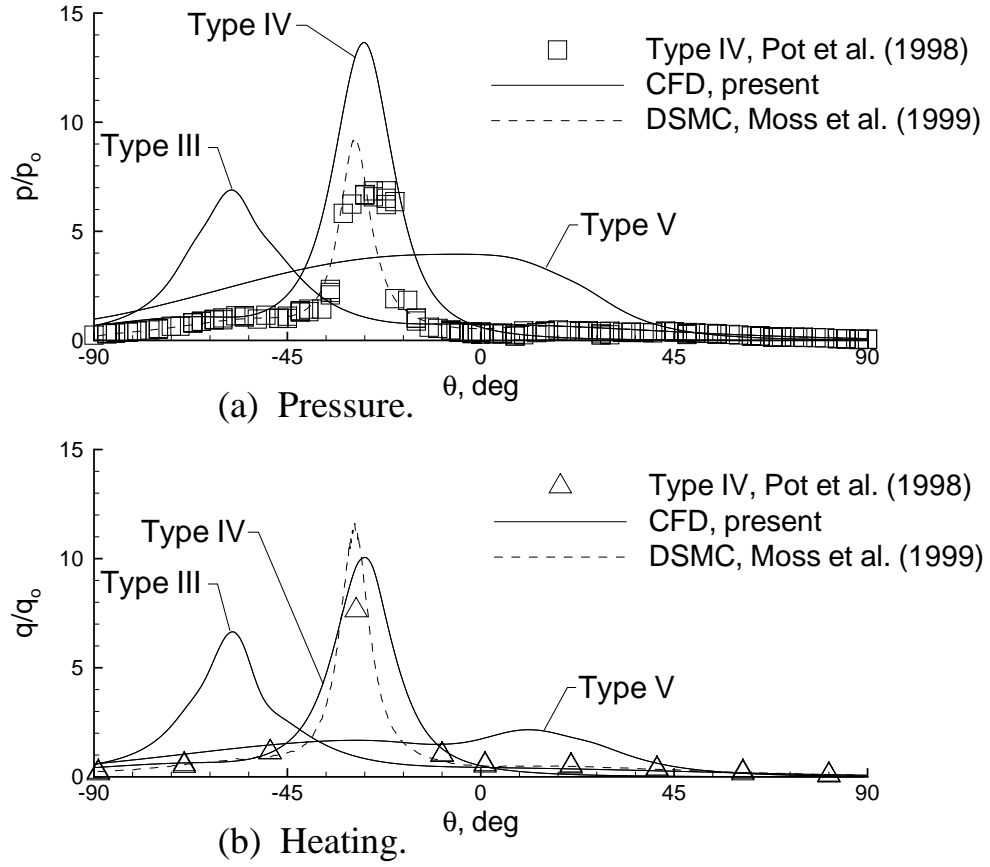


Figure 9: Effect of shock-wave interference type on surface properties.

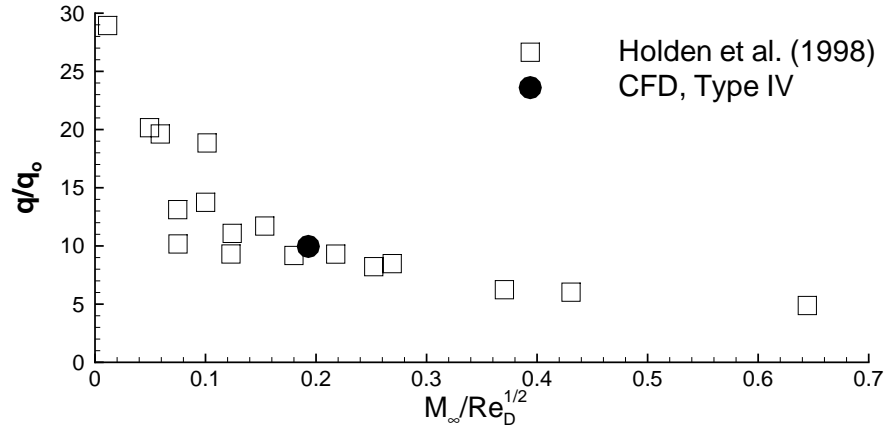


Figure 10: Comparison of present Type IV results with the correlation of [4].

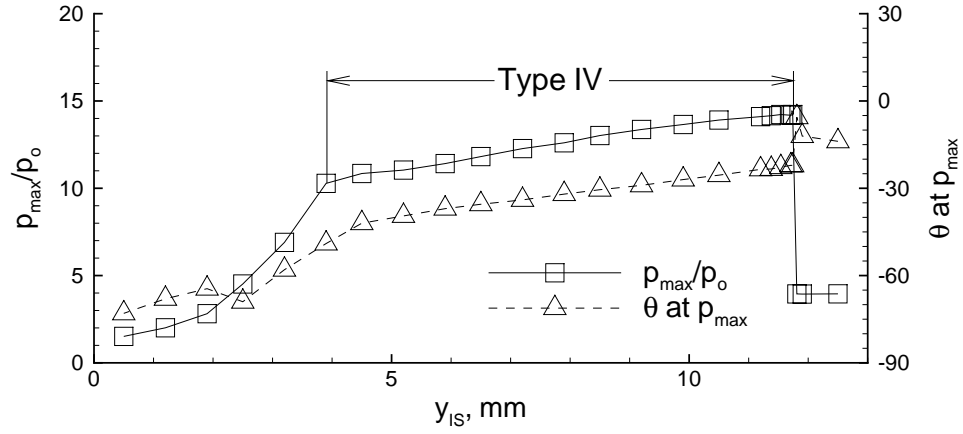


Figure 11: Interaction maximum surface pressure and location as a function of incident shock position, y_{IS} .

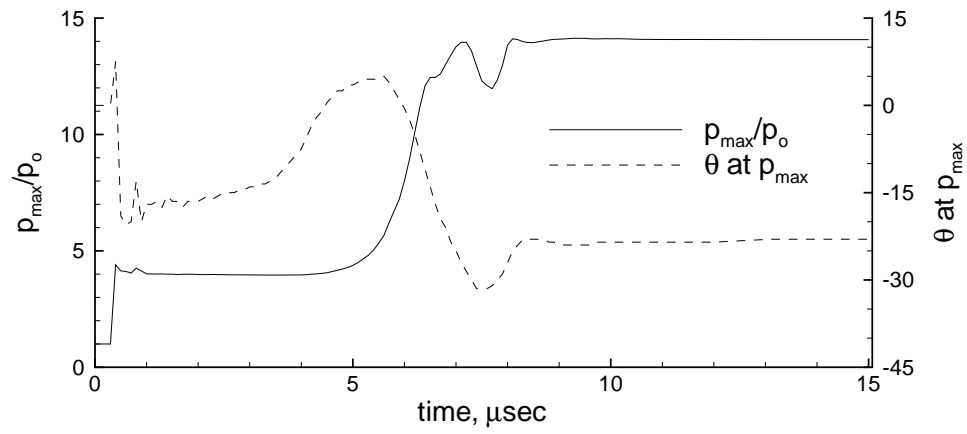


Figure 12: Maximum surface pressure and location for time accurate CFD of Type IV interference.

REPORT DOCUMENTATION PAGE			Form Approved OMB No. 0704-0188	
Public reporting burden for this collection of information is estimated to average 1 hour per response, including the time for reviewing instructions, searching existing data sources, gathering and maintaining the data needed, and completing and reviewing the collection of information. Send comments regarding this burden estimate or any other aspect of this collection of information, including suggestions for reducing this burden, to Washington Headquarters Services, Directorate for Information Operations and Reports, 1215 Jefferson Davis Highway, Suite 1204, Arlington, VA 22202-4302, and to the Office of Management and Budget, Paperwork Reduction Project (0704-0188), Washington, DC 20503.				
1. AGENCY USE ONLY (Leave blank)		2. REPORT DATE July 1999		3. REPORT TYPE AND DATES COVERED Technical Memorandum
4. TITLE AND SUBTITLE Numerical Simulation of Low-Density Shock-Wave Interactions			5. FUNDING NUMBERS 242-80-01-01	
6. AUTHOR(S) Christopher E. Glass				
7. PERFORMING ORGANIZATION NAME(S) AND ADDRESS(ES) NASA Langley Research Center Hampton, VA 23681-2199			8. PERFORMING ORGANIZATION REPORT NUMBER L-17878	
9. SPONSORING/MONITORING AGENCY NAME(S) AND ADDRESS(ES) National Aeronautics and Space Administration Washington, DC 20546-0001			10. SPONSORING/MONITORING AGENCY REPORT NUMBER NASA/TM-1999-209358	
11. SUPPLEMENTARY NOTES				
12a. DISTRIBUTION/AVAILABILITY STATEMENT Unclassified-Unlimited Subject Category 34 Distribution: Standard Availability: NASA CASI (301) 621-0390			12b. DISTRIBUTION CODE	
13. ABSTRACT (Maximum 200 words) CFD numerical simulations of low-density shock-wave interactions for an incident shock impinging on a cylinder have been performed. Flow-field density gradient and surface pressure and heating define the type of interference pattern and corresponding perturbations. The maximum pressure and heat transfer level and location for various interaction types (i.e., shock-wave incidence with respect to the cylinder) are presented. A time-accurate solution of the Type IV interference is employed to demonstrate the establishment and the steadiness of the low-density flow interaction.				
14. SUBJECT TERMS shock-wave interference patterns, shock/shock interaction, Type IV interference, Edney interaction, supersonic jet impingement			15. NUMBER OF PAGES 22	
			16. PRICE CODE A03	
17. SECURITY CLASSIFICATION OF REPORT Unclassified	18. SECURITY CLASSIFICATION OF THIS PAGE Unclassified	19. SECURITY CLASSIFICATION OF ABSTRACT Unclassified	20. LIMITATION OF ABSTRACT	